Journal of Materials Chemistry A

Investigation of Rh-titanate ($ATiO_3$) interactions on high-surface-area perovskites thin films prepared by atomic layer deposition

Journal:	*Journal of Materials Chemistry A*
Manuscript ID	TA-ART-06-2020-005981.R1
Article Type:	Paper
Date Submitted by the Author:	24-Jul-2020
Complete List of Authors:	Lin, Chao; University of Pennsylvania, Chemical and Biomolecular Engineering Foucher, Alexandre ; University of Pennsylvania, Materials Science and Engineering Ji, Yichen ; University of Pennsylvania, Chemical and Biomolecular Engineering Stach, Eric; University of Pennsylvania, Materials Science and Engineering Gorte, Raymond; University of Pennsylvania, Chemical and Biomolecular Engineering

Investigation of Rh-titanate ($ATiO_3$) interactions on high-surface-area perovskites thin films prepared by atomic layer deposition

*Chao Lin [a], Alexandre C. Foucher [b], Yichen Ji [a], Eric A. Stach [b] & Raymond J. Gorte [a, *]*

[a] Department of Chemical and Biomolecular Engineering, University of Pennsylvania, 34th Street, Philadelphia, PA 19104, United States

[b] Department of Materials Science and Engineering, University of Pennsylvania, Philadelphia, PA 19104, United States

KEYWORDS

CO oxidation; Atomic Layer Deposition (ALD); "Intelligent" catalyst; Rh catalyst; $CaTiO_3$, $SrTiO_3$, $BaTiO_3$, perovskites.

ABSTRACT

Thin, ~1-nm films of $CaTiO_3$, $SrTiO_3$, and $BaTiO_3$ were deposited onto $MgAl_2O_4$ by Atomic Layer Deposition (ALD) and studied as catalyst supports for Rh. Scanning Transmission Electron Microcopy (STEM) and X-Ray Diffraction (XRD) demonstrated that the films had the perovskite structure and formed uniform coatings stable to 1073 K. Rh, added by ALD, interacted strongly with $CaTiO_3$ and somewhat less strongly with $SrTiO_3$, while Rh on $BaTiO_3$ was similar to Rh on unmodified $MgAl_2O_4$. STEM measurements of Rh on $CaTiO_3$ films showed Rh remained well dispersed after repeated oxidations and reductions at 1073 K; however, the Rh was inactive for CO-oxidation. Rh formed small particles on $SrTiO_3$ films and was active for CO oxidation after reduction at 1073 K. The reducibility and catalytic activity of $Rh/BaTiO_3/MgAl_2O_4$ were similar to that of $Rh/MgAl_2O_4$. Evidence from CO-TPR, FTIR, and XPS all indicated that the degree of interaction between Rh and the three perovskite films can be ranked in the following order: $Rh/CaTiO_3/MgAl_2O_4$ > $Rh/SrTiO_3/MgAl_2O_4$ > $Rh/BaTiO_3/MgAl_2O_4$. Bulk ex-solution catalysts, synthesized by reduction of $ATi_{0.98}Rh_{0.02}O_3$ (A=Ca, Sr, and Ba), were also examined for comparison.

Introduction

Metal-doped perovskites have been referred to as "Intelligent Catalysts" because the metals can be redispersed by oxidation treatments, followed by high-temperature reduction [1-5]. Redispersion occurs when the metal atoms become part of the perovskite lattice during oxidation, then exsolve as metal particles egress from the lattice upon reduction. Although the concept was initially applied to automotive, emissions-control catalysts [3, 5], it has more recently been applied to other, high-temperature applications, including Solid Oxide Fuel Cell (SOFC) electrodes [6-8] and reforming catalysts[9-11]. Unfortunately, there are major problems that prevent the wide-scale application of the approach for catalysis. First, because most perovskites cannot be maintained as high-surface-area materials, the metal catalysts based on perovskite supports will have low surface areas[12, 13]. Second, it has been shown that the kinetics of metal ingress into the lattice is sluggish, making the redispersion process ineffective in at least some cases [14-16]. Third, in at least some cases, much of the metal that exsolves from the lattice remains embedded in the bulk of the perovskite, inaccessible to gas-phase reactants [14, 17].

To avoid the problems associated with encapsulation of metal particles in the bulk perovskite, as well as to increase rates for the possible ingress and egress of metals into the oxide lattice, our group has been growing the perovskites as thin films on more stable supports using Atomic Layer Deposition. Uniform films of $LaFeO_3$ [18, 19], $CaTiO_3$ [20, 21], and $LaCoO_3$ [22] films have been grown on $MgAl_2O_4$ supports, with film thicknesses ranging from 0.5 to 1.2 nm. With the exception of $LaCoO_3$ after high-temperature reduction, the films appear to be very stable to both oxidizing and reducing conditions at temperatures as high as 1073 K. Some metal catalysts on thin-film perovskite supports exhibited low activity following high-temperature oxidation and high activity after high-temperature reduction, similar to what would be expected if the metals were going in and out of the perovskite lattice [18, 20, 22].

While the focus of most studies on perovskite supports has been on a possible exsolution process, recent work has revealed that strong support effects with perovskite-supported metals can influence the properties of the metal in other ways. For example, a study of Ni on $LaFeO_3$ films indicated that interfacial contact between the two phases altered the thermodynamics of Ni oxidation by significantly stabilizing NiO [19]. In a study of the Pt/$CaTiO_3$ system, Pt particles supported on both thin-film and bulk $CaTiO_3$ showed very low activity for toluene hydrogenation, despite being highly active for CO oxidation [20]. The interactions in these two cases also appear to

be related to the perovskite structure, since Ni and Pt supported on the individual oxides that make up the perovskites do not exhibit unusual properties. Other evidence for a relationship between exsolution phenomena and strong support interactions came from a comparison of Pt and Pd on $CaTiO_3$ thin films. With bulk perovskites, it has been reported that Pt can enter the $CaTiO_3$ lattice while Pd cannot [3]. While catalysts formed by Pt on thin-film $CaTiO_3$ showed evidence of strong support effects, Pd/$CaTiO_3$ was not distinct from Pd catalysts on non-interacting supports [20]. However, because the perovskite film thicknesses in these studies were much less than the typical metal particle size observed in ex-solution, there must also be differences between the thin-film catalysts and those formed by bulk ex-solution.

In the present study, we first demonstrate the successful preparation of 1-nm films of $CaTiO_3$, $SrTiO_3$, and $BaTiO_3$ on $MgAl_2O_4$. The prepared films showed good thermal stability and remained uniform upon high temperature treatments. We compared support effects on Rh due to contact with these three perovskite films. Although these three perovskites are similar, we show that changing the A-site cation leads to very significant changes in the reducibility, activity, and sintering properties of the Rh, with the degree of interaction decreasing dramatically in going from Rh/$CaTiO_3$/$MgAl_2O_4$ to Rh/$SrTiO_3$/$MgAl_2O_4$ and Rh/$BaTiO_3$/$MgAl_2O_4$. Finally, we compare the properties of the thin film supports with their bulk counterparts and show that there are significant differences.

Experimental Methods

All ALD-prepared catalysts used in this study were supported on $MgAl_2O_4$ that was prepared in our laboratory and described in more detail elsewhere [18]. The sample had a surface area of 120 m^2/g and its XRD pattern showed only the characteristic peaks for the spinel structure. The equipment used for ALD is also described in detail elsewhere [23-25]. The system is essentially a high-temperature adsorption unit that can be evacuated with a mechanical vacuum pump. The evacuated $MgAl_2O_4$ samples could then be exposed to vapors from the precursor or an oxidant. For precursors that were difficult to oxidize, the sample could also be removed from the system and oxidized in a muffle furnace. Growth rates were measured gravimetrically.

For comparison purposes, bulk Rh-doped perovskites, $ATi_{0.98}Rh_{0.02}O_3$ (A=Ca, Sr, and Ba) were synthesized using sol-gel procedures. The corresponding A-site nitrate (either $Ca(NO_3)_2•(H_2O)_4$ (Sigma-Aldrich), $Sr(NO_3)_2$, (Sigma-Aldrich), or $Ba(NO_3)_2$, (Alfa Aesar)) was

dissolved into an aqueous solution containing $[CH_3CH(O-)CO_2NH_4]_2Ti(OH)_2$ (Dihydroxybis (ammonium lactato) titanium solution, Alfa Aesar) and $Rh(NO_3)_4 \cdot xH_2O$ (Rhodium(III) nitrate hydrate, Alfa Aesar). After adding stoichiometric amounts of citric acid (Fisher Chemical), the solution was heated to form a viscous gel. After drying, the resulting powder was crushed and placed in a muffle furnace at 1373 K for 6 h to form the perovskite phases.

X-ray diffraction (XRD) patterns were recorded on a Rigaku MiniFlex diffractometer equipped with a Cu Kα source ($\lambda = 0.15416$ nm). ICP-OES were performed on a Spectro Genesis spectrometer with a concentric nebulizer. Samples were first dissolved in 10 ml of *aqua regia* at 333 K overnight, after which the solutions were diluted to a suitable concentration range.

Ex-situ, Scanning Transmission Electron Microscopy (STEM) measurements were performed on powder specimens that had been diluted in isopropanol and then deposited onto carbon support films on copper grids (Electron Microscopy Sciences). Imaging and elemental mapping via energy dispersive X-ray Spectroscopy (EDS) were performed with a JEOL NEOARM operated at 200 kV.

Surface areas for samples prepared by ALD were measured using BET isotherm in a homemade apparatus [23], while surface areas for the bulk perovskites were calculated from their crystallite sizes, determined from XRD. Metal dispersions were estimated using CO chemisorption at room temperature, assuming a stoichiometry of one CO per Rh, even though the CO:Rh stoichiometry is known to depend on Rh particle size [24, 25]. For these measurements, the samples were first pretreated in a flow reactor at the desired conditions before being transferred to the adsorption apparatus. Within the adsorption system, the samples were reduced in 400 Torr H_2 for 30 min at 473 K to remove any oxide formed by exposure to air in transferring the sample from the flow reactor to the adsorption system.

Temperature-Programmed Desorption/Thermogravimetric Analysis (TPD-TGA) was carried out in a system that has been described in detail elsewhere [26]. The system is built around a CAHN 2000 microbalance and a quadrupole mass spectrometer (SRI RGA-100) and could be evacuated to 10^{-8} Torr with a turbomolecular pump. In a typical measurement, 50-mg samples were heated in a vacuum to 823 K, then exposed to the vapor of 2-propanol (99.9%, Fisher, USA) at room temperature. After 1-h evacuation, TPD-TGA measurements were performed using a temperature ramp of 10 K/min.

CO-oxidation rates were determined under differential conversions in a 0.25-inch, quartz, tubular-flow reactor at atmospheric pressure, with products analyzed using a gas chromatograph (SRI 8610C) equipped with a TCD detector. The catalyst loadings were 100 mg for the ALD-prepared samples and 1 g for the bulk perovskite samples. The total gas flow rate was maintained at 120 mL min^{-1}, with partial pressures of 25 torr CO and 12.5 Torr O_2, the balance being He. To investigate the stability of the materials under redox conditions, the samples were oxidized in flowing 10% O_2:He mixtures at 1073 K for 1 h and reduced in 10% H_2:He mixtures at the same temperature.

Reducibility of the samples were determine by flow titration, as described in detail elsewhere [27]. These experiments were performed in a flow reactor at 1 atm, with a quadrupole mass spectrometer for continuous monitoring of the effluent. 500-mg samples were first reduced in pure H_2 at 1073 K using a flow rate of 20 mL min^{-1}. After purging the sample with He, the sample was exposed to dry air at 1073 K and a flow rate of 5 mL min^{-1}. The O_2 uptake was then determined by integrating the difference between the N_2 and O_2 signals in the mass spectrometer. Temperature-Programmed Reduction (TPR) measurements were performed in the same system. Prior to these experiments, the 500-mg samples were oxidized in dry air for 1 h at 1073 K. The TPR measurements were then performed using 10% CO:He mixtures, with a total flow rate of 20 mL min^{-1} and a heating rate of 10 K min^{-1} from 298 to 1073 K.

X-Ray Photoelectron Spectra (XPS) were acquired on a Physical Electronics Versa Probe 5000 (ULVAC-PHI, Inc., Japan) Spectrometer using Al-Kα monochromatic X-rays. Diffuse Reflectance Fourier Transform Infrared Spectra (DRIFTS) for CO stretching were collected on a Mattson Galaxy FTIR with a diffuse-reflectance attachment (DiffusIR™, Pike Technologies).

Results

Preparation of Thin-Film Perovskites

ALD was used to grow 1-nm films of $CaTiO_3$, $SrTiO_3$, and $BaTiO_3$ on the $MgAl_2O_4$. The precursors for the A-site cations, Ca, Sr, and Ba, were bis(2,2,6,6-tetramethyl-3,5-heptanedionato) calcium ($Ca(TMHD)_2$, Strem, USA), bis(2,2,6,6-tetramethyl-3,5-heptanedionato) strontium hydrate ($Sr(TMHD)_2$, Strem, USA) and bis(2,2,6,6-tetramethyl-3,5-heptanedionato) barium hydrate ($Ba(TMHD)_2$, Strem, USA). Titanium chloride ($TiCl_4$, Sigma-Aldrich, USA) was used to deposit Ti. For deposition of the A-site cations, 0.5-g samples were evacuated, exposed to the

precursor vapors for 10 min at 573 K, and then evacuated again. Because it was not possible to remove the TMHD ligands by oxidation at 573 K, the samples were removed from the system and placed in a muffle furnace at 773 K for 5 min before returning them to the ALD system. Ti deposition was performed at 423 K and Cl was removed by simply exposing the sample to water vapor at that temperature.

Growth rates for the various precursors were determined gravimetrically and confirmed by Inductively Couple Plasma-Optical Emission Spectroscopy (ICP-OES). For CaO and TiO_2, the sample weights were previously shown to increase linearly with the number of ALD cycles, with growth rates of 6.9×10^{13} Ca/cm^2-cycle (0.015 nm CaO/cycle) and 9.9×10^{13} Ti/cm^2-cycle (0.025 nm TiO_2/cycle) [20]. The growth rates did not change when deposition alternated between Ca and Ti, and samples with the correct Ca:Ti ratio could be prepared by depositing six cycles of Ca for every four cycles of Ti. The sample weights also increased linearly with the number of ALD cycles for Sr and Ba, as shown in Figures S1 of the Supplemental Information; however, in order to reconcile the weight changes with the compositions obtained from ICP-OES, it was necessary to assume that $SrCO_3$ and $BaCO_3$ were formed initially. On that basis, the growth rates for Sr and Ba were 3.6×10^{13} Sr/cm^2-cycle and 3.7×10^{13} Ba/cm^2-cycle. The Ti growth rates were not affected by the probable presence of carbonates; and formation of $BaTiO_3$ and $SrTiO_3$ films was achieved by depositing six cycles of either Sr or Ba, followed by two cycles of TiO_2. Growth rates for $SrTiO_3$ and $BaTiO_3$ films are shown in figure S2.

After depositing the prerequisite amounts of perovskite precursors, the samples were heated to 1073 K in a muffle furnace in order to form the perovskite phases. In the cases of $SrTiO_3$ and $BaTiO_3$, a loss of sample weight was observed following calcination, consistent with decomposition of carbonates. The targeted thickness for each mixed-oxide film in this study was 1-nm. Assuming the densities of the films were the same as that of the corresponding bulk perovskites and that the 120-m^2/g $MgAl_2O_4$ was uniformly covered, this required loadings ranging from 32-wt% for $CaTiO_3$ to 42-wt% for $BaTiO_3$. A list of these samples and their bulk counterparts is given in Table 1 along with some of their key properties. It is noteworthy that the A:Ti ratio for each of the films was within 8% of the correct value for the corresponding perovskites.

Table 1. key properties for bulk perovskite materials and ALD samples

	A:Ti ratio from ICP-OES analysis	Specific surface area (m^2/g) after 1073 K calcination	ALD thin film loading
$CaTi_{0.98}Rh_{0.02}O_3$	-	11 [a]	-
$SrTi_{0.98}Rh_{0.02}O_3$	-	8 [a]	-
$BaTi_{0.98}Rh_{0.02}O_3$	-	8 [a]	-
$CaTiO_3/MgAl_2O_4$	0.93	84	30 wt% [b]
$SrTiO_3/MgAl_2O_4$	1.08	71	34 wt% [b]
$BaTiO_3/MgAl_2O_4$	1.01	64	41 wt% [b]
Ca-ALD/$MgAl_2O_4$	-	63	23 wt% [c]
Sr-ALD/$MgAl_2O_4$	-	77	16 wt% [b]
Ba-ALD/$MgAl_2O_4$	-	73	21 wt% [b]
Ti-ALD/$MgAl_2O_4$	-	95	38 wt% [c]

a: sample surface areas were estimated from crystal size given by Scherrer equation
b: sample loadings estimated from ICP-OES
c: sample loadings estimated from weight gains after ALD cycles

Characterization of Perovskite ALD Films

To determine the morphology of the ALD films, the $CaTiO_3/MgAl_2O_4$, $SrTiO_3/MgAl_2O_4$, and $BaTiO_3/MgAl_2O_4$ samples listed in Table 1 were analyzed by STEM/EDS, TPD-TGA measurements of 2-propanol, and XRD. To ensure that the films were well crystallized, each of the samples was calcined at 1073 K prior to any measurements. The STEM/EDS results for $CaTiO_3/MgAl_2O_4$ were reported elsewhere [21], while the analogous results for $SrTiO_3/MgAl_2O_4$ and $BaTiO_3/MgAl_2O_4$ are shown in Figure 1. The micrographs were similar in all three cases. The $MgAl_2O_4$ showed features in the 10-20nm size range but there were no discernable changes upon addition of the films, even though the weight loadings of the films ranged from 30- to 41-wt%. The EDS mappings were similarly featureless and showed that both Ti and the alkali metals covered the surfaces uniformly. This implies that the component oxides for each perovskite were

well mixed on the surface following deposition and that there was no agglomeration of the films into particles, even after heat treatments at 1073 K.

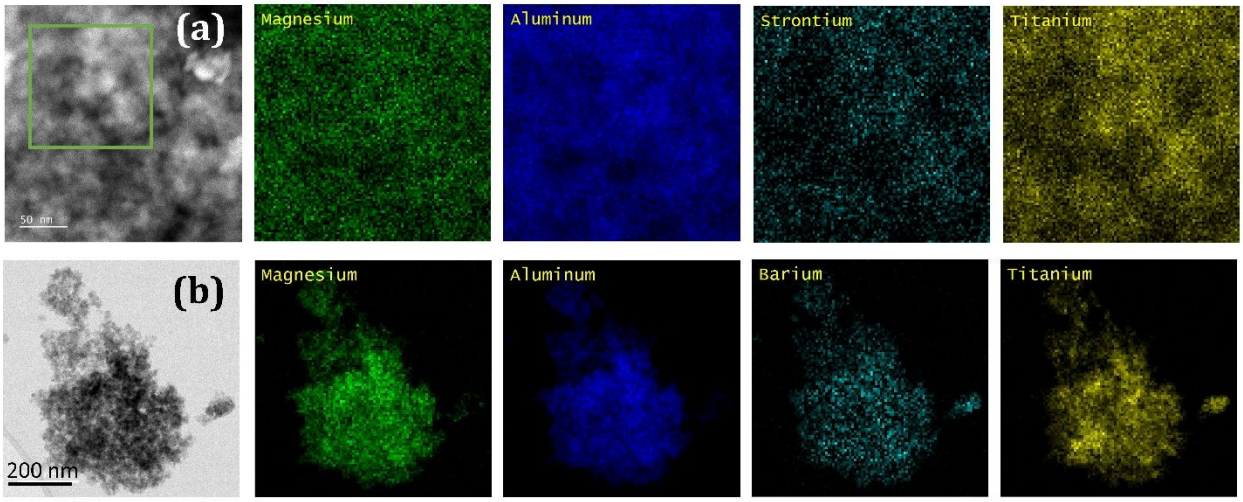

Figure 1. Representative STEM results for (a) $SrTiO_3/MgAl_2O_4$ (b) $BaTiO_3/MgAl_2O_4$ after 1073K oxidation with EDS maps of corresponding elements.

Additional evidence for film uniformity was obtained from the TPD-TGA profiles of 2-propanol shown in Figure 2. Measurements on each of the samples were performed after exposure to 2-propanol vapor at room temperature, followed by 1-h evacuation. On $MgAl_2O_4$, 680 μmol/g of 2-propanol remained on the surface following evacuation, corresponding to 3.3×10^{18} molecules/m^2 for the 120-m^2/g sample. This is close to what would be expected for a monolayer, implying that the entire surface was probed by the adsorbate. For purposes of this study, it is important to notice that all of the adsorbed alcohol desorbs below 500 K, with a significant fraction desorbing as propene (m/e = 41) in a very sharp feature at 460 K. The additional weight change at higher temperatures was due to water desorption, which occurred over a broad temperature range. The reaction of 2-propanol on $MgAl_2O_4$ is due to the Lewis acidity of the surface [28, 29].

The analogous TPD-TGA results for $CaTiO_3/MgAl_2O_4$, $SrTiO_3/MgAl_2O_4$, and $BaTiO_3/MgAl_2O_4$ were significantly different. The initial coverages after exposure and 1-h evacuation were slightly lower on these three samples, ranging from 2.0 to 2.8×10^{18} molecules/m^2, but still close to that expected for a monolayer. However, the fractions of 2-propanol which desorbed unreacted were significantly higher and the reaction temperatures increased with the mass of the alkali cation. The peak reaction temperature on $CaTiO_3/MgAl_2O_4$ was 600 K; on

$BaTiO_3/MgAl_2O_4$, there was essentially no reaction. If any of the $MgAl_2O_4$ had remained uncovered, a reaction peak below 500 K should have been observed, implying that the mixed oxide films must completely cover the support surface. The higher peak temperatures and lower reactivity of the $CaTiO_3/MgAl_2O_4$, $SrTiO_3/MgAl_2O_4$, and $BaTiO_3/MgAl_2O_4$ samples is consistent with a decrease in Lewis-acid strength of these surfaces. It is also potentially significant that TiO_2 was also added last in our ALD synthesis of $CaTiO_3/MgAl_2O_4$, $SrTiO_3/MgAl_2O_4$, and $BaTiO_3/MgAl_2O_4$. TiO_2 has Lewis acidity and a previous study showed that TPD-TGA results for 2-propanol from ALD-prepared $TiO_2/MgAl_2O_4$ were very similar to that of $MgAl_2O_4$ [20]. If the mixed-oxide films were simply a simple sum of TiO_2 and the alkali oxide, with TiO_2 at the outer surface, reaction of the 2-propanol at lower temperatures should have been observed.

As discussed earlier, the targeted film thickness was 1-nm for each of these samples and the weight loadings correspond to that value. Since this is only a two-unit-cell thickness of the corresponding perovskites, film uniformity implies that most of the deposited material must be present in the films. If a significant number of larger particles were present, there would not be sufficient material to still cover the surface of the $MgAl_2O_4$ support.

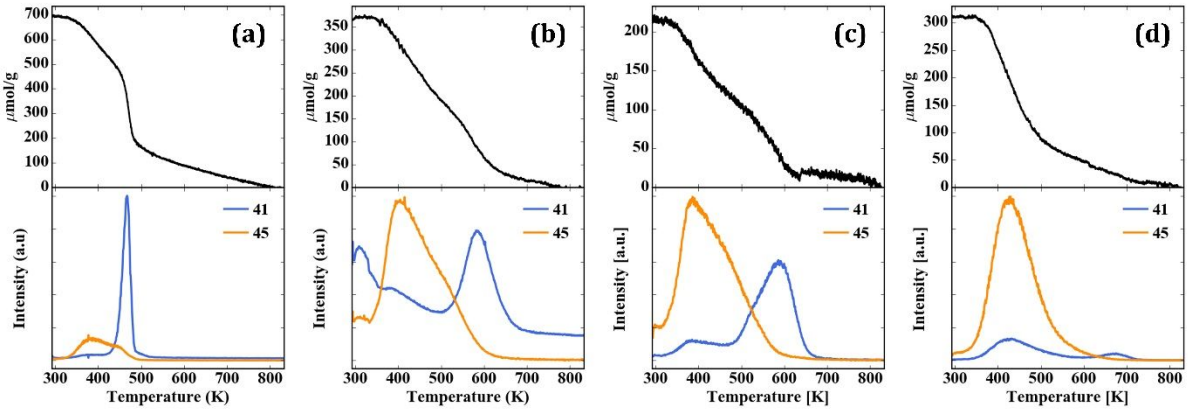

Figure 2. TPD-TGA profiles for 2-propanol. Samples had been calcined at 1073 K for 3 h: (a) $MgAl_2O_4$, (b) $CaTiO_3/MgAl_2O_4$, (c) $SrTiO_3/MgAl_2O_4$ and (d) $BaTiO_3/MgAl_2O_4$. Desorption features correspond to propene (m/e=41) and unreacted 2-propanol (m/e=45 and 41).

XRD patterns for the $CaTiO_3/MgAl_2O_4$, $SrTiO_3/MgAl_2O_4$, and $BaTiO_3/MgAl_2O_4$ samples are shown in Figure 3, with the pattern for $MgAl_2O_4$ shown at the bottom for comparison. In each case, all of the peaks can be assigned to either the $MgAl_2O_4$ support or the corresponding perovskite phase. For $BaTiO_3/MgAl_2O_4$, there is significant overlap in the peak positions for

$BaTiO_3$ and $MgAl_2O_4$; however, the relative ratio of peaks, particularly those centered at 32 and 37 degrees 2θ, make it clear that the XRD pattern for $BaTiO_3/MgAl_2O_4$ is due to a mixture of $MgAl_2O_4$ and the perovskite structure. In order to determine whether the relative intensities of XRD peaks are consistent with the loading of the perovskite films, Rietveld Analysis was performed on the $CaTiO_3/MgAl_2O_4$ sample after it had been redox cycled five times at 1073 K in order to ensure complete crystallization of the perovskite phase. The results of this analysis are shown in Figure S3 and Table S2. No additional peaks were observed following the redox treatments but the peaks associated with the perovskite phase were somewhat narrower. Rietveld analysis indicated the loading of the $CaTiO_3$ phase to be 24-wt%, only slightly lower than the ICP value of 30-wt%.

Estimations of the average crystallite size of the thin $CaTiO_3$ and $SrTiO_3$ films using the Scherrer Equation gave values of ~ 20 nm. However, the presence of a significant concentration of three-dimensional crystallites this large is inconsistent with the uniform coverage of the $MgAl_2O_4$ support seen by STEM and 2-propanol TPD. As discussed in more detail elsewhere [30], the perovskite phase is likely present as randomly oriented platelets. The crystallite size associated with the diffraction linewidths is then the in-plane dimension of the two-dimensional crystallites.

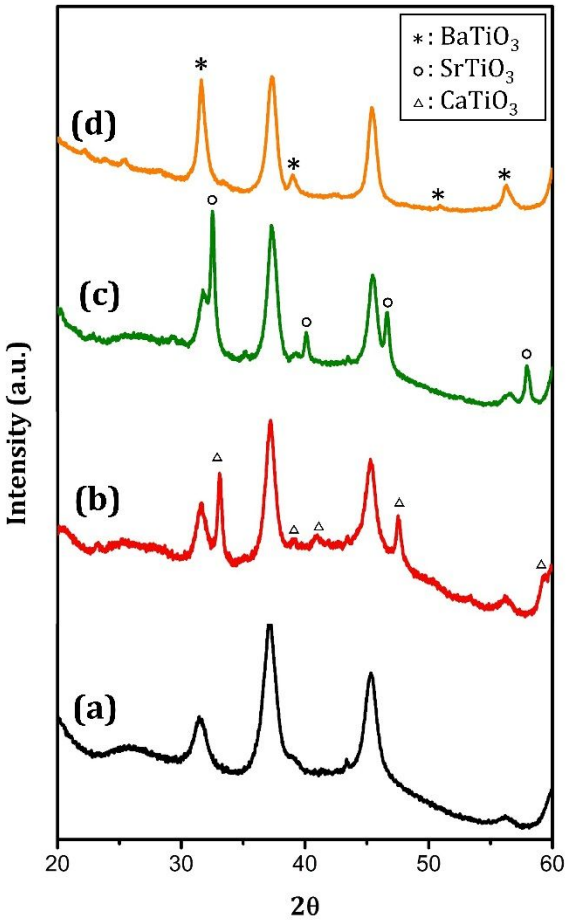

Figure 3. XRD patterns for (a) $MgAl_2O_4$, (b) $CaTiO_3/MgAl_2O_4$, (c) $SrTiO_3/MgAl_2O_4$ and (d) $BaTiO_3/MgAl_2O_4$ after 1073 K oxidation.

Characterization of Rh Particles on Perovskite ALD Films

Rh was added to each of the supports by ALD using Rhodium(III) acetylacetonate ($Rh(acac)_3$, Strem, USA). The procedure was similar to that used to deposit the alkali cations, except that the deposition temperature was 523 K. Removal of the ligands was again achieved by calcining the samples in a muffle furnace at 773 K. Because the growth rate for Rh was ~1.3×10^{14} Rh/cm^2-cycle on each of the samples, a single ALD cycle was sufficient to achieve a metal loading of close to 2-wt%. The properties of these samples are listed in Table 2.

Table 2. Key features of the added Rh for various samples

	Rh loading confirmed by ICP-OES (wt%)	Dispersion values by CO chemisorption after redox cycles with the final treatment being:	
		573 K reduction	1073 K reduction
$Rh/MgAl_2O_4$	2.0	10%	25%
$Rh/CaTiO_3/MgAl_2O_4$	2.1	0%	0%
$Rh/SrTiO_3/MgAl_2O_4$	2.1	17%	20%
$Rh/BaTiO_3/MgAl_2O_4$	1.8	14%	23%
$Rh/CaO/MgAl_2O_4$	-	27%	32%
$Rh/TiO_2/MgAl_2O_4$	-	3%	21%*

*To avoid effects of SMSI, the dispersion here was measured after the same was reduced at high temperatures, oxidized at 673 K, then reduced at 673 K.

As an initial indication of how Rh interacts with the three perovskite films, STEM measurements were performed on the first four Rh-containing samples reported in Table 2. In each case, the Rh was added by 1 ALD cycle and the samples were then oxidized and reduced five times at 1073 K, with the 1073-K reduction being the last step. A STEM image of the $Rh/MgAl_2O_4$ sample, shown in Figure S4, indicates Rh particles ranging in size from 1 to 10 nm. This range of particle sizes agrees reasonably well with the Rh dispersion determined from CO chemisorption, reported in Table 2.

The STEM images and EDS maps for Rh on the $CaTiO_3/MgAl_2O_4$, $SrTiO_3/MgAl_2O_4$, and $BaTiO_3/MgAl_2O_4$ supports, reported in Figure 4, were significantly different. Even after this relatively harsh redox cycling, we were unable to detect Rh particles in the STEM images of the $Rh/CaTiO_3/MgAl_2O_4$ sample, Figure 4a). EDS mapping showed that the Rh was uniformly distributed over the sample and gave a bulk concentration that was in good agreement with elemental analysis, suggesting that the Rh must exist as particles less than about 1 nm in size. It is noteworthy that this does not agree with the very low dispersion measurements reported in Table 2 for this catalyst. CO did not appreciably adsorb on this sample.

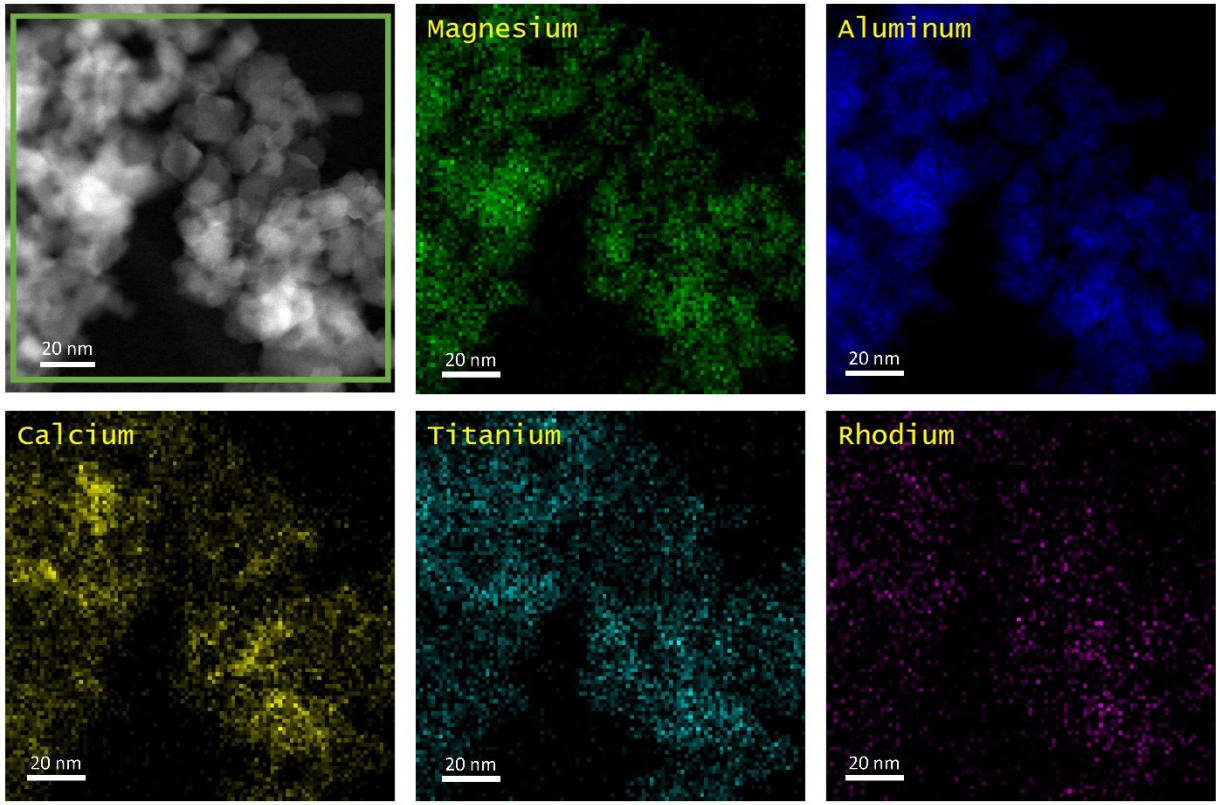

Figure 4a. Representative STEM/EDS results for $Rh/CaTiO_3/MgAl_2O_4$ after five 1073 K redox cycles with the final treatment being reduction.

Small Rh particles were found on the $Rh/SrTiO_3/MgAl_2O_4$ sample, Figure 4b). The particles were very uniform in size and about 1-2 nm in diameter. This is slightly smaller than the particle size calculated from CO chemisorption measurements, which gave values on the order of 5 nm, suggesting that adsorption may be somewhat suppressed in the same way as we observed on the $Rh/CaTiO_3/MgAl_2O_4$ sample. Finally, the STEM image of the $Rh/BaTiO_3/MgAl_2O_4$, Figure 4c), was similar to that measured on the $Rh/MgAl_2O_4$. The sample contained a large distribution of particle sizes, ranging from 2- to 10-nm in diameter, in good agreement with the particle-size estimated from CO chemisorption.

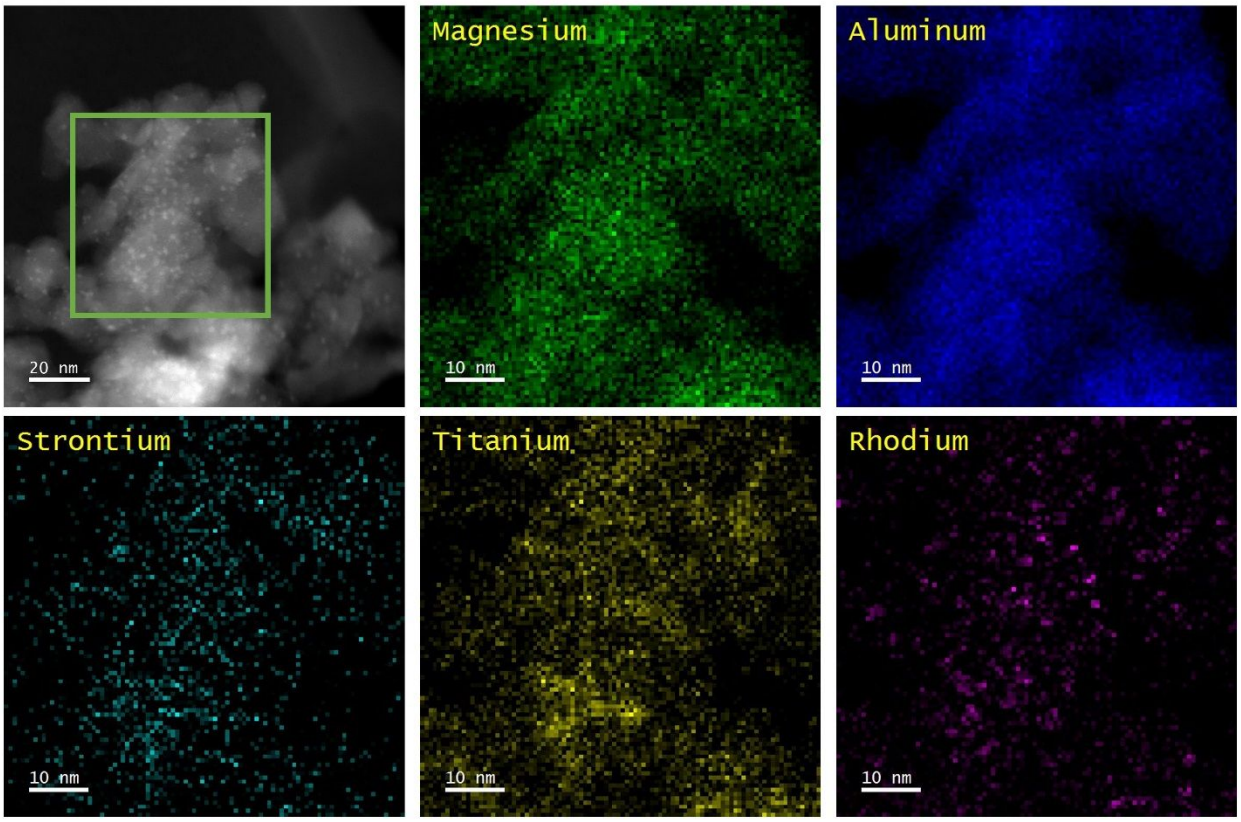

Figure 4b. Representative STEM/EDS results for $Rh/SrTiO_3/MgAl_2O_4$ after five 1073 K redox cycles with the final treatment being reduction.

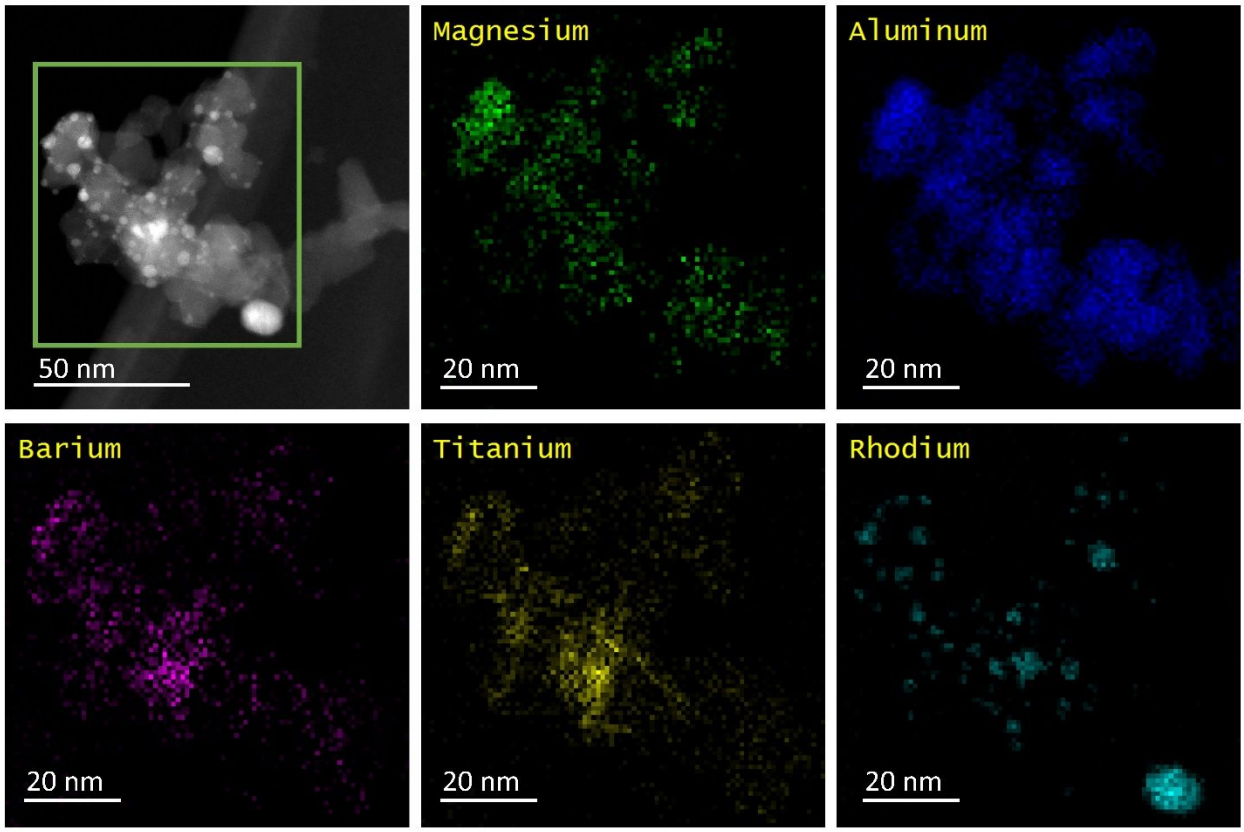

Figure 4c. Representative STEM/EDS results for $Rh/BaTiO_3/MgAl_2O_4$ after five 1073 K redox cycles with the final treatment being reduction.

An indication of the differences in the Rh particles on the various supports can also be seen from the DRIFTS measurements in Figure 5. Rh single-atom catalysts exhibit the symmetric and asymmetric stretches of a dicarbonyl species, while larger Rh particles show peaks associated with terminal- and bridge-bonded CO [25]. Consistent with the STEM results, DRIFTS data for the $Rh/MgAl_2O_4$ and $Rh/BaTiO_3/MgAl_2O_4$, Figures 5a) and 5d), show the expected terminal-bonded (~2083 cm^{-1}) and bridge-bonded (~1855 cm^{-1}) species. Consistent with the small amount of CO adsorption on $Rh/CaTiO_3/MgAl_2O_4$, Figure 5b, only very weak vibrational bands were observed on this sample. In agreement with the small particle size observed with $Rh/SrTiO_3/MgAl_2O_4$, the DRIFTS results, Figure 5c, exhibit intense peaks at 2017 cm^{-1} and 2090 cm^{-1}, indicative of adsorption as a dicarbonyl. The one surprising aspect of this result is the Rh dispersion on this sample, obtained from CO adsorption and reported in Table 2, was only 20%, assuming a stoichiometry of one CO per Rh. With formation of a dicarbonyl, the CO:Rh ratio should be two.

If all of the Rh were indeed exposed, we should have expected CO uptakes ten times that which we observed.

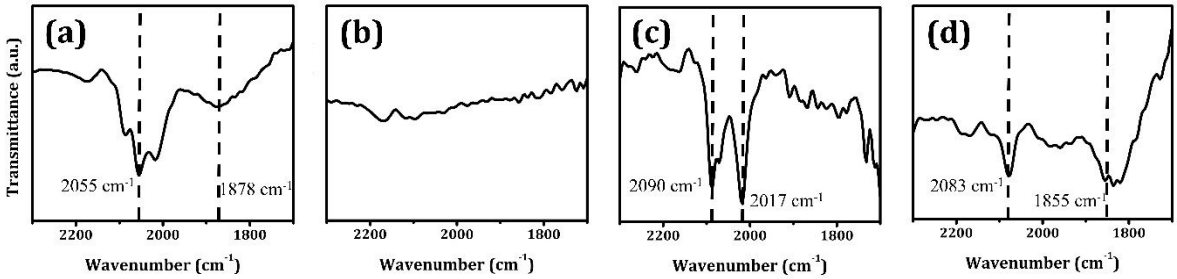

Figure 5. FTIR spectra for (a) $Rh/MgAl_2O_4$, (b) $Rh/CaTiO_3/MgAl_2O_4$, (c) $Rh/SrTiO_3/MgAl_2O_4$, and (d) $Rh/BaTiO_3/MgAl_2O_4$ after exposure to CO at room temperature after five 1073 K redox cycles with the final treatment being reduction.

Finally, to eliminate the possibility that the low CO adsorption coverages on $Rh/CaTiO_3/MgAl_2O_4$ are due to Rh interactions with either CaO or TiO_2, DRIFTS measurements were performed on the Rh that had been deposited on films of either CaO or TiO_2 on $MgAl_2O_4$. The pretreatment conditions on these samples were the same as that used on the perovskite films and the final treatment was again a reduction step at 1073 K. The results are shown in Figure S5. For $Rh/CaO/MgAl_2O_4$ in Figure S5, the spectra show dicarbonyl stretches indicative of small Rh particles, together with a large carbonate band centered at 1875 cm^{-1}. The DRIFT spectrum for $Rh/TiO_2/MgAl_2O_4$ is representative of CO stretching on larger Rh particles, with a peak at 2075 cm^{-1} being the strongest signal. The fact that we can detect CO stretching for Rh deposited on the individual CaO and TiO_2 samples provides additional evidence that suppression of CO adsorption on $CaTiO_3/MgAl_2O_4$ is related in some way to the perovskite structure.

CO Oxidation Rates

To determine how the different perovskite films affect catalytic properties, CO-oxidation activities were obtained on each of the thin-film catalysts, as well as the bulk ex-solution catalysts. Again, each of the thin-film catalysts was aged by five redox cycles at 1073 K, but the final step before rate measurements was the 1073-K oxidation step. Because high-temperature reduction is required to activate ex-solution catalysts, differential rates were measured after no reduction, reduction in 10% H_2 for 1 h at 573 K, and reduction for 1 h at 1073 K. Rates were measured in 25 Torr CO and 12.5 Torr O_2 and are shown in Figure 6. On the oxidized $Rh/MgAl_2O_4$, Figure 6a),

rates were initially low but increased upon reduction at 573 K and even more after reduction at 1073 K. Clearly, the oxidized Rh is not as active as metallic Rh and 573 K was not sufficient to completely reduce the larger Rh particles supported on $MgAl_2O_4$. The normalized rates on the reduced $Rh/MgAl_2O_4$ were essentially identical to what has been reported in previous work [31, 32].

The analogous results on $Rh/CaTiO_3/MgAl_2O_4$ are shown in Figure 6b). The rates on this catalyst were initially lower than that on $Rh/MgAl_2O_4$ and did not increase significantly upon reduction at either 573 or 1073 K. The rates on the reduced $Rh/CaTiO_3/MgAl_2O_4$ catalysts were more than a factor of 20 lower than those on reduced $Rh/MgAl_2O_4$. Rate data for $Rh/SrTiO_3/MgAl_2O_4$ in Figure 6c) were similar to what was observed on $Rh/MgAl_2O_4$, with rates increasing with reduction temperature, as well as being very similar in magnitude after reduction at 1073 K. As shown in Figure 6d), the $Rh/BaTiO_3/MgAl_2O_4$ appears to already be completely reduced at 573 K and reduction at higher temperatures did not significantly change the rates.

To determine whether the catalytic properties are affected if the perovskite is B-site deficient, we deposited three additional ALD cycles of CaO onto the $CaTiO_3/MgAl_2O_4$ sample to determine whether this would affect the properties of the supported Rh. Figure S6 shows that a $Rh/CaTiO_3/MgAl_2O_4$ sample with a nominal Ca:Ti stoichiometry of 1.1 exhibited catalytic rates that were essentially the same as what is shown in figure 6b.

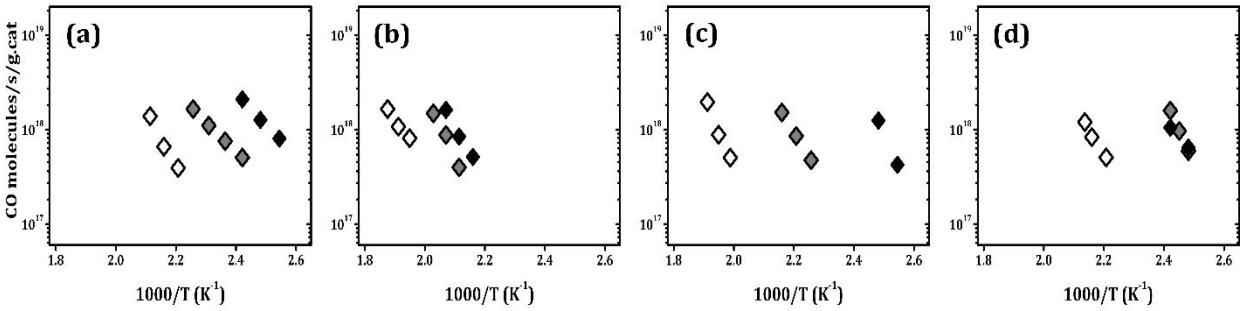

Figure 6. Steady-state, differential reaction rates for CO oxidation with 25 Torr of CO and 12.5 Torr O_2 for (a) $Rh/MgAl_2O_4$, (b) $Rh/CaTiO_3/MgAl_2O_4$, (c) $Rh/SrTiO_3/MgAl_2O_4$, and (d) $Rh/BaTiO_3/MgAl_2O_4$ as a function of reduction temperature. Reduction pretreatment temperature: (white) no reduction, (grey) 573 K reduction, and (black) 1073 K reduction.

To eliminate the possibility that the low catalytic activity of $Rh/CaTiO_3/MgAl_2O_4$ came from one of the individual components that make up $CaTiO_3$, rates were measured on the

$Rh/CaO/MgAl_2O_4$ and $Rh/TiO_2/MgAl_2O_4$ samples, with results reported in Figure S7. For $Rh/CaO/MgAl_2O_4$, the activity was essentially the same as with $Rh/MgAl_2O_4$. The catalyst was easily reduced at 573 K and exhibited similar rates. Rates on $Rh/TiO_2/MgAl_2O_4$ were somewhat lower than that observed on either $Rh/MgAl_2O_4$ or $Rh/CaO/MgAl_2O_4$ after high temperature reduction, probably due to an "SMSI" effect in which the Rh particles are partially covered by TiO_2. However, both single-component catalysts were significantly more active than $Rh/CaTiO_3/MgAl_2O_4$.

It is interesting to compare Rh on the thin-film perovskites to Rh ex-solving from the bulk counterparts. Results for CO oxidation on $CaTi_{0.98}Rh_{0.02}O_3$, $SrTi_{0.98}Rh_{0.02}O_3$, and $BaTi_{0.98}Rh_{0.02}O_3$ are shown as a function of the reduction temperature in Figure 7. Because the surface areas of these materials were much lower, the catalyst loadings were ten times higher and the rates are shown on a different scale, even though the Rh loadings are much higher. Unlike the case with the thin-film perovskites, rates on the three bulk samples were very similar. Without reduction, each showed very low activity. Reduction at 573 K increased rates by a factor roughly ten and reduction at 1173 K increased rates by another factor of ten, almost certainly due to Rh being brought to the surface.

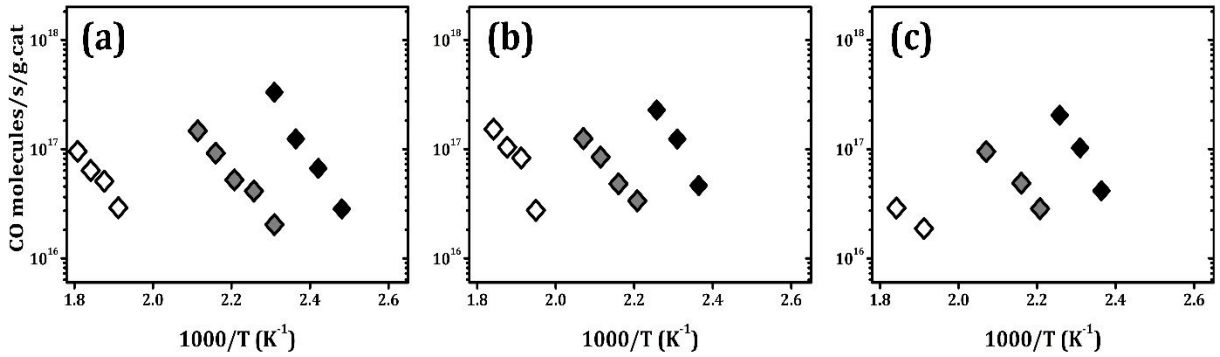

Figure 7. Steady-state, differential reaction rates for CO oxidation with 25 Torr of CO and 12.5 Torr O_2 for (a) $CaTi_{0.98}Rh_{0.02}O_3$, (b) $SrTi_{0.98}Rh_{0.02}O_3$, and (c) $BaTi_{0.98}Rh_{0.02}O_3$ as a function of reduction temperature. Reduction pretreatment temperature: (white) no reduction, (grey) 573 K reduction, and (black) 1173 K reduction.

Rh Oxidation State

To determine whether Rh is being completely reduced in the thin-film perovskite catalysts, flow-titration measurements were performed to determine the amount of oxygen that could be

taken up by catalysts at 1073 K after they had been reduced in flowing, 10% H_2 for 1 h at either 573 or 1073 K. These results are reported in Table 3. Oxygen uptakes on each of the support materials were negligible, even after reduction at 1073 K. Only the $BaTiO_3/MgAl_2O_4$ and $TiO_2/MgAl_2O_4$ samples showed any measurable uptake; and, even for this sample, the uptake was a small fraction of the uptakes on the Rh-containing samples. Since each of the Rh-containing catalysts were approximately 2-wt% Rh (2.0-wt% = 194 μmol Rh/g), complete oxidation of metallic Rh to Rh_2O_3 corresponds to ~300 μmol O/g. For $Rh/MgAl_2O_4$, Rh reduction at 573 K was incomplete but the O:Rh stoichiometry after reduction at 1073 K matched well that expected for the Rh-Rh_2O_3 transition. Results for $Rh/BaTiO_3/MgAl_2O_4$ differed from that of $Rh/MgAl_2O_4$ only in that reduction was nearly complete after 573 K. $Rh/SrTiO_3/MgAl_2O_4$ appears to have been more difficult to reduce and the total oxygen uptake was slightly less than that expected for a completely reduced catalyst, even after reduction at 1073 K.

However, while results for $Rh/SrTiO_3/MgAl_2O_4$ after reduction at 1073 K were close to that expected theoretically, results for $Rh/CaTiO_3/MgAl_2O_4$ clearly did not match the theoretical oxygen uptakes. Even after reduction at 1073 K, the oxygen uptake was only 100 μmol/g, a third of the theoretical value. Reducibilities of $Rh/CaO/MgAl_2O_4$ and $Rh/TiO_2/MgAl_2O_4$ were similar to those that were expected, demonstrating again that support effects with the $CaTiO_3$ perovskite film were different from that of the individual oxides making up $CaTiO_3$.

Table 3. Results from oxygen titration for various samples

	Oxygen uptake for samples after different reduction pretreatments (atomic O)	
	573K reduction	1073K reduction
$MgAl_2O_4$	-	0
$CaTiO_3/MgAl_2O_4$	-	0
$SrTiO_3/MgAl_2O_4$	-	10
$BaTiO_3/MgAl_2O_4$	-	30
$CaO/MgAl_2O_4$	-	0
$TiO_2/MgAl_2O_4$	-	50
$Rh/MgAl_2O_4$	170	300
$Rh/CaTiO_3/MgAl_2O_4$	50	100
$Rh/SrTiO_3/MgAl_2O_4$	110	260
$Rh/BaTiO_3/MgAl_2O_4$	260	300
$Rh/CaO/MgAl_2O_4$	-	280
$Rh/TiO_2/MgAl_2O_4$	-	330

*Rh loading ~2wt% (194 μmol/g)

The reduction kinetics for the $Rh/MgAl_2O_4$, $Rh/CaTiO_3/MgAl_2O_4$, $Rh/SrTiO_3/MgAl_2O_4$, and $Rh/BaTiO_3/MgAl_2O_4$ were also quantified by CO TPR measurements, with results given in Figure 8. The Rh on $MgAl_2O_4$ reduced in two temperature regions, reacting in peaks centered at 580 K and 810 K. The 580-K peak is almost certainly associated with reduction of Rh near the surface of the Rh particles. Because this sample also has larger Rh particles, the second peak may be due to reduction of the bulk oxide. The TPR data for $Rh/BaTiO_3/MgAl_2O_4$ were very similar to that of $Rh/MgAl_2O_4$; but $Rh/SrTiO_3/MgAl_2O_4$ reduction was clearly more sluggish, with peaks shifted to higher temperatures. Since the Rh particle size on the $Rh/SrTiO_3/MgAl_2O_4$ samples were small, it seems unlikely that the increased peak temperatures are due to bulk reduction, again suggesting some kind of interaction between Rh and the $SrTiO_3$. In agreement with the flow-titration data, much less oxygen could be removed from the $Rh/CaTiO_3/MgAl_2O_4$ sample and all reduction that did occur happened at high temperatures. Again, TPR profiles for $Rh/CaO/MgAl_2O_4$ and $Rh/TiO_2/MgAl_2O_4$, shown Figure S8, were dissimilar from $Rh/CaTiO_3/MgAl_2O_4$.

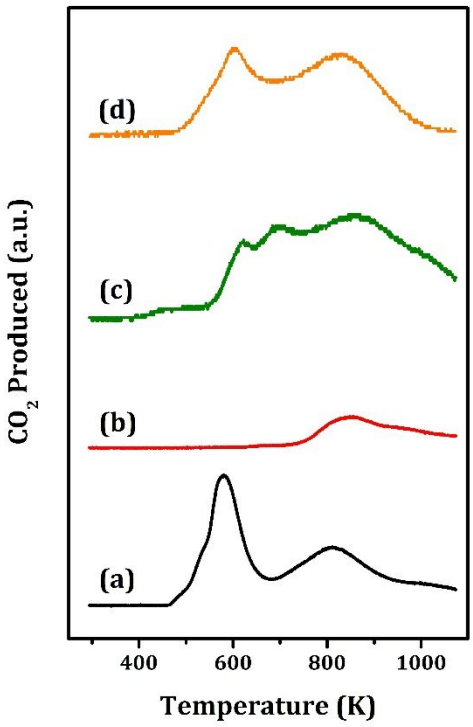

Figure 8. CO-TPR profile for (a) $Rh/MgAl_2O_4$, (b) $Rh/CaTiO_3/MgAl_2O_4$, (c) $Rh/SrTiO_3/MgAl_2O_4$, and (d) $Rh/BaTiO_3/MgAl_2O_4$.

Because the flow-titration measurements only determine the change in oxygen content in going from reducing to oxidizing conditions, it is possible that the $Rh/CaTiO_3/MgAl_2O_4$ is never completely oxidized. To gain additional insights into the Rh oxidation states, XPS spectra were measured on the $Rh/CaTiO_3/MgAl_2O_4$, $Rh/SrTiO_3/MgAl_2O_4$, and $Rh/BaTiO_3/MgAl_2O_4$ samples, with results shown in Figure 9 for both oxidized and reduced samples. For all three samples, there is a shift of around 1.6 eV between oxidized and reduced samples, suggesting a change in oxidation states between Rh^{3+} and Rh^0. For the reduced samples, the Rh peaks for the $Rh/BaTiO_3/MgAl_2O_4$ sample were centered at 306.7 eV and 311.4 eV and can be assigned to the metallic Rh doublet ($3d_{5/2}$ and $3d_{3/2}$). The Rh spectrum for $Rh/SrTiO_3/MgAl_2O_4$ is almost identical to that of $Rh/BaTiO_3/MgAl_2O_4$, again implying an oxidation state of Rh^0. The XPS spectrum for Rh on the reduced $Rh/CaTiO_3/MgAl_2O_4$ was shifted 0.6 eV shift towards higher energy level, probably due to final-state effects [33], since the shift was also observed in the oxidized samples.

Obviously, there is an apparent discrepancy between the oxygen uptakes observed in the redox measurements and the XPS results for the $Rh/CaTiO_3/MgAl_2O_4$ sample. A possible explanation for the discrepancy, as well as for the low catalytic activity of this sample, is that the reduced Rh is moving subsurface to the $CaTiO_3$-$MgAl_2O_4$ interface. There is some evidence for this from the Rh:A-site cation peak ratios shown in Table 4. The Rh:Ca ratio decreased by a factor of roughly 10 upon sample reduction. Since the STEM images indicated the dispersion is high in both cases, the reduction in Rh peak intensity cannot be due to an increase in particle size. Since the mean-free-path for electrons in XPS is typically less than 1 nm, migration of Rh below the perovskite film should result in a significant reduction in the Rh XPS peak intensity. The presence of metallic Rh in the bulk of the support could also change the O:Rh stoichiometry. Finally, the Rh:A-site cation intensities for the $Rh/SrTiO_3/MgAl_2O_4$ and $Rh/BaTiO_3/MgAl_2O_4$ samples are easily explained by formation of reduced Rh particles at the perovskite surfaces upon reduction. For $Rh/SrTiO_3/MgAl_2O_4$, the Rh particles are very small so that all of the reduced Rh is essentially at the surface. For $Rh/BaTiO_3/MgAl_2O_4$, the Rh signal is reduced due to the formation of very large Rh particles.

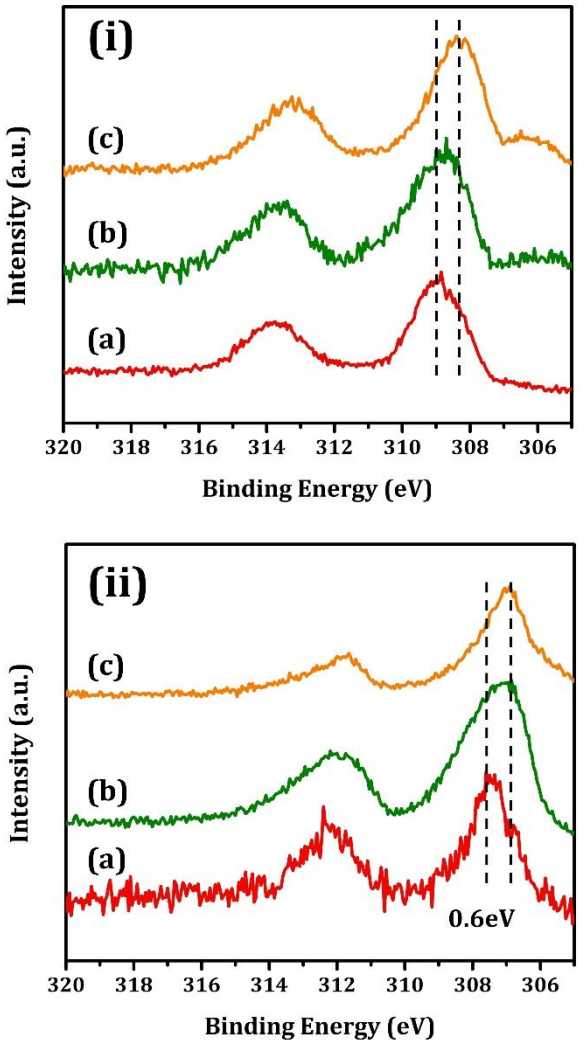

Figure 9. XPS spectra for Rh (3d) region for (a) $Rh/CaTiO_3/MgAl_2O_4$, (b) $Rh/SrTiO_3/MgAl_2O_4$, and (c) $Rh/BaTiO_3/MgAl_2O_4$ after five 1073-K redox cycles with the final treatment being (i)oxidation and (ii) reduction.

Table 4. Rh: A-site Cation XPS area ratio comparison

Sample	Rh: A-site Cation XPS area ratio*	
	Oxidized	Reduced
$Rh/CaTiO_3/MgAl_2O_4$	0.70	0.06
$Rh/SrTiO_3/MgAl_2O_4$	0.40	0.96
$Rh/BaTiO_3/MgAl_2O_4$	0.48	0.16

*: Rh 3d (~307 eV), Ca 2p (~347 eV), Sr 3d (~133 eV), and Ba 3d (~780 eV) signals were used for integration.

Discussion

The results of this study raise interesting questions about the nature of metal-support interactions with perovskites and about differences between bulk and surface perovskites. We will address each of these points below.

It is important first to address the question of differences and similarities between bulk and surface perovskites as supports for metal catalysts. Past work has shown that there are at least some similarities. For example, with bulk catalysts, it is expected that high-temperature oxidation will drive the metal into the lattice and that high-temperature reduction would then be required to bring metal back to the surface and restore activity. Similar to this, activity is low after high-temperature oxidation and restored only upon high-temperature reduction in many of the thin-film catalysts our group has investigated [18, 20, 22]. Second, with Ni-based reforming catalysts, both bulk and thin-film catalysts show greatly increased tolerance against coking [19, 21]. Third, both bulk and thin-film catalyst exhibit specificity (e.g. Pd shows negligible interactions with $CaTiO_3$ films [20] and does not enter the bulk $CaTiO_3$ lattice [3].). Finally, Pt-$CaTiO_3$ thin-film and bulk catalysts that were highly active for CO oxidation showed low activity for toluene hydrogenation [20].

However, it is not surprising that metals ex-solved from bulk perovskites would also show important differences from metals on thin-films when the film thickness is less than the particle diameter. In the present study, $Rh/CaTiO_3$ catalysts prepared by ex-solution from bulk perovskites were catalytically very active, both in this work and in past studies [16], while the thin-film version was inactive. The reasons for the low activity of $Rh/CaTiO_3/MgAl_2O_4$ are not completely clear since the Rh remained very well dispersed. The flow-titration data suggest that the Rh may not be completely reduced, but that in itself is unusual behavior given the ease with which Rh is normally reduced and the severe reducing conditions that were used in the present study. Based on this

explanation, one would also expect the bulk catalyst to be similarly difficult to reduce. An alternative explanation is that Rh migrates to the $CaTiO_3$-$MgAl_2O_4$ interface at some point during the catalyst treatment and remains subsurface upon reduction. While this would not prevent observation of Rh by XPS given the perovskite film thickness is similar to the expected mean-free-path of electrons [34], the Rh:Ca intensity ratio is expected to be lower since Rh is subsurface. In fact, this is exactly what we observe.

Specific support interactions in perovskite-supported catalysts are often neglected, perhaps in part because the ex-solved metal particles are so large that the surface metal atoms are not affected by the support [35]. It is not surprising that metal-perovskite interactions will be important for smaller particles, given the specificity that has previously been demonstrated [3]. Indeed, the ex-solution process itself may be different in some systems. For example, with Ni ex-solution from $La_xSrNiTiO_x$ [36, 37], Ni particles nucleate in the bulk and migrate to the surface, while extrusion of Pd nanowires was reported for Pd-$BaCeO_3$ system [38].

It is interesting that perovskites as similar as $CaTiO_3$, $SrTiO_3$, and $BaTiO_3$ would exhibit such strong differences in their thin-film versions. One possibility is that differences in the surface energies of the different perovskites changes the interaction energies with Rh. Evidence for differences between the perovskites was show clearly by the isopropanol TPD-TGA results. From previous Low Energy Ion Scattering (LEIS) measurements, the $CaTiO_3$ films were shown to be A-site terminated [20]. With the larger cations, the surface may be B-site terminated. Finally, the free volumes for these three perovskite materials change with the size of the cations. Taking the free volume to be the difference in volumes of the perovskite cell and the volume of all anions and cations in that cell, $CaTiO_3$ has the largest free volume of around 80%. All these differences could be related to differences of surface energies in thin film perovskites.

There is obviously much that we still need to learn about both ex-solution catalysts and about the differences between bulk and thin-film perovskites. It is almost certain that the behaviors we observed were thermodynamically-driven, and factors such as metal-perovskite combination selections, relative sizes between doped metals and perovskites, and addition of a third component (high-surface-area supports) can all contribute to the changes of thermally-stable state at given conditions. Thermodynamic understanding for all these systems can certainly lead to better catalyst design. But whatever the mechanism is, demonstration of high-surface area perovskites leads to

the creation of systems that permited us to better explore the relationships between structure and catalytic properties.

Conclusions

Important differences were observed for Rh catalysts supported on 1-nm films of $CaTiO_3$, $SrTiO_3$, and $BaTiO_3$ on $MgAl_2O_4$. Large Rh particles were formed after redox cycling at 1073 K when Rh was supported on $MgAl_2O_4$ or $BaTiO_3$ films; however, Rh formed only small particles on $SrTiO_3$ films and appeared to remain almost atomically dispersed on $CaTiO_3$ films. Rh catalysts prepared from the $CaTiO_3$ films exhibited very low activity for CO oxidation, possibly because the Rh resides under the $CaTiO_3$ surface. Interestingly, the large differences observed for the thin film catalysts were not observed when Rh was ex-solved from the bulk perovskites, suggesting that there may be important differences between thin-film and bulk perovskites.

FOOTNOTES

ALD growth rates, results from Rietveld analysis of the XRD patterns, catalytic performance of Rh on $CaTiO_3$ films with excess Ca, and single-component ALD oxides performance can be found in the supporting information.

CORRESPONDING AUTHOR

gorte@seas.upenn.edu

FUNDING SOURCES

Department of Energy, Office of Basic Energy Sciences, Chemical Sciences, Geosciences and Biosciences Division, Grant No. DE-FG02-13ER16380

ACKNOWLEDGMENT

C.L. and R.J.G. are grateful to the Department of Energy, Office of Basic Energy Sciences, Chemical Sciences, Geosciences and Biosciences Division, Grant No. DE-FG02-13ER16380 for support of this work. A.C.F. and E.A.S. acknowledge support from the Vagelos Institute for Energy Science and Technology through a graduate fellowship to A.C.F. Electron microscopy was carried out at the Singh Center for Nanotechnology at the University of Pennsylvania which is supported by the National Science Foundation (NSF) National Nanotechnology Coordinated Infrastructure Program grant NNCI-1542153, with additional support from the University of Pennsylvania Materials Research Science and Engineering Center (MRSEC) grant supported by the National Science Foundation (DMR-1720530)

CONFLICTS OF INTEREST

There are no conflicts to declare.

REFERENCES

1. Y. Nishihata, J. Mizuki, T. Akao, H. Tanaka, M. Uenishi, M. Kimura, T. Okamoto and N. Hamada, *Nature*, 2002, **418**, 164.
2. H. Tanaka, I. Tan, M. Uenishi, M. Kimura and K. Dohmae, *Topics in Catalysis*, 2001, **16**, 63-70.
3. H. Tanaka, M. Taniguchi, M. Uenishi, N. Kajita, I. Tan, Y. Nishihata, J. i. Mizuki, K. Narita, M. Kimura and K. Kaneko, *Angewandte Chemie International Edition*, 2006, **45**, 5998-6002.
4. H. Tanaka, M. Uenishi, M. Taniguchi, I. Tan, K. Narita, M. Kimura, K. Kaneko, Y. Nishihata and J. i. Mizuki, *Catalysis Today*, 2006, **117**, 321-328.
5. M. Uenishi, M. Taniguchi, H. Tanaka, M. Kimura, Y. Nishihata, J. Mizuki and T. Kobayashi, *Applied Catalysis B: Environmental*, 2005, **57**, 267-273.
6. A. Marcucci, F. Zurlo, I. N. Sora, E. Placidi, S. Casciardi, S. Licoccia and E. Di Bartolomeo, *Journal of Materials Chemistry A*, 2019, **7**, 5344-5352.
7. T. Zhu, H. E. Troiani, L. V. Mogni, M. Han and S. A. Barnett, *Joule*, 2018, **2**, 478-496.
8. Y. Gao, D. Chen, M. Saccoccio, Z. Lu and F. Ciucci, *Nano Energy*, 2016, **27**, 499-508.
9. M. Seo, S. Y. Kim, Y. D. Kim, E. D. Park and S. Uhm, *International Journal of Hydrogen Energy*, 2018, **43**, 11355-11362.
10. D. Papargyriou, D. N. Miller and J. T. S. Irvine, *Journal of Materials Chemistry A*, 2019, **7**, 15812-15822.
11. U. Oemar, M. Ang, W. Hee, K. Hidajat and S. Kawi, *Applied Catalysis B: Environmental*, 2014, **148**, 231-242.
12. P. Steiger, O. Kröcher and D. Ferri, *Applied Catalysis A: General*, 2020, **590**, 117328.
13. H. Arandiyan, Y. Wang, J. Scott, S. Mesgari, H. Dai and R. Amal, *ACS Applied Materials and Interfaces*, 2018, **10**, 16352-16357.
14. M. B. Katz, S. Zhang, Y. Duan, H. Wang, M. Fang, K. Zhang, B. Li, G. W. Graham and X. Pan, *Journal of Catalysis*, 2012, **293**, 145-148.
15. S. Zhang, M. B. Katz, S. Dai, K. Zhang, X. Du, G. W. Graham and X. Pan, *The Journal of Physical Chemistry C*, 2017, **121**, 17348-17353.
16. S. A. Malamis, R. J. Harrington, M. B. Katz, D. S. Koerschner, S. Zhang, Y. Cheng, L. Xu, H.-W. Jen, R. W. McCabe and G. W. Graham, *Catalysis Today*, 2015, **258**, 535-542.
17. K. J. Kim, H. Han, T. Defferriere, D. Yoon, S. Na, S. J. Kim, A. M. Dayaghi, J. Son, T.-S. Oh and H. M. Jang, *Journal of the American Chemical Society*, 2019.
18. T. M. Onn, M. Monai, S. Dai, E. Fonda, T. Montini, X. Pan, G. W. Graham, P. Fornasiero and R. J. Gorte, *Journal of the American Chemical Society*, 2018, **140**, 4841-4848.
19. X. Mao, A. C. Foucher, E. A. Stach and R. J. Gorte, *Journal of Catalysis*, 2020, **381**, 561-569.
20. C. Lin, A. C. Foucher, Y. Ji, C. D. Curran, E. A. Stach, S. McIntosh and R. J. Gorte, *ACS Catalysis*, 2019, **9**, 7318-7327.
21. C. Lin, J. B. Jang, L. Zhang, E. A. Stach and R. J. Gorte, *ACS Catalysis*, 2018, **8**, 7679-7687.
22. X. Mao, A. C. Foucher, E. A. Stach and R. J. Gorte, *Inorganics*, 2019, **7**, 113.
23. T. M. Onn, S. Zhang, L. Arroyo-Ramirez, Y.-C. Chung, G. W. Graham, X. Pan and R. J. Gorte, *ACS Catalysis*, 2015, **5**, 5696-5701.
24. Y. Tang, C. Asokan, M. Xu, G. W. Graham, X. Pan, P. Christopher, J. Li and P. Sautet, *Nature Communications*, 2019, **10**, 1-10.

25. J. Yates Jr, T. Duncan, S. Worley and R. Vaughan, *The Journal of Chemical Physics*, 1979, **70**, 1219-1224.
26. Y. Ji, J. Pan, P. Dauenhauer and R. J. Gorte, *Applied Catalysis A: General*, 2019, **577**, 107-112.
27. T. M. Onn, X. Mao, C. Lin, C. Wang and R. J. Gorte, *Inorganics*, 2017, **5**, 69.
28. Y.-L. Shan, T. Wang, Z.-J. Sui, Y.-A. Zhu and X.-G. Zhou, *Catalysis Communications*, 2016, **84**, 85-88.
29. J. Luo, J. Yu, R. J. Gorte, E. Mahmoud, D. G. Vlachos and M. A. Smith, *Catalysis Science & Technology*, 2014, **4**, 3074-3081.
30. X. Mao, A. C. Foucher, T. Montini, E. A. Stach, P. Fornasiero and R. J. Gorte, *Journal of the American Chemical Society*, 2020, **142**, 10373-10382.
31. J. A. Anderson, *Journal of the Chemical Society, Faraday Transactions*, 1991, **87**, 3907-3911.
32. M. A. Newton, A. J. Dent, S. Diaz-Moreno, S. G. Fiddy, B. Jyoti and J. Evans, *Chemistry–A European Journal*, 2006, **12**, 1975-1985.
33. Y. V. Larichev, B. L. Moroz and V. I. Bukhtiyarov, *Applied Surface Science*, 2011, **258**, 1541-1550.
34. J. M. Paige, Y. Cheng, P. A. Pepin, C. D. Curran, D. Sun, M. U. Chen, S. McIntosh, J. M. Vohs and R. J. Gorte, *Solid State Ionics*, 2019, **341**, 115051.
35. I. Ro, J. Resasco and P. Christopher, *ACS Catalysis*, 2018, **8**, 7368-7387.
36. D. Neagu, T.-S. Oh, D. N. Miller, H. Ménard, S. M. Bukhari, S. R. Gamble, R. J. Gorte, J. M. Vohs and J. T. Irvine, *Nature Communications*, 2015, **6**, 8120.
37. T.-S. Oh, E. K. Rahani, D. Neagu, J. T. Irvine, V. B. Shenoy, R. J. Gorte and J. M. Vohs, *The Journal of Physical Chemistry Letters*, 2015, **6**, 5106-5110.
38. J. Li, U. G. Singh, J. W. Bennett, K. Page, J. C. Weaver, J.-P. Zhang, T. Proffen, A. M. Rappe, S. Scott and R. Seshadri, *Chemistry of Materials*, 2007, **19**, 1418-1426.

GRAPHICAL ABSTRACT